

Ferroelectricity in Hafnia: The Origin of Nanoscale Stabilization

Xin Li^{1*}, Guodong Ren^{2*}, Haidong Lu¹, Kartik Samanta¹, Amit Kumar Shah¹, Pravan Omprakash², Yu Yun¹, Pratyush Buragohain¹, Huibo Cao³, Jordan A. Hachtel⁴, Andrew R. Lupini⁴, Miaofang Chi⁴, Evgeny Y. Tsybal^{1,5}✉, Alexei Gruverman^{1,5}✉, Rohan, Mishra^{2,6}✉, Xiaoshan Xu^{1,5}✉

¹Department of Physics and Astronomy, University of Nebraska, Lincoln, NE 68588, USA

²Institute of Materials Science and Engineering, Washington University in St. Louis, St. Louis, MO 63130, USA

³Neutron Scattering Division, Oak Ridge National Lab, Oak Ridge, TN 37830, USA

⁴Center for Nanophase Materials Sciences, Oak Ridge National Lab, Oak Ridge, TN 37830, USA

⁵Nebraska Center for Materials and Nanoscience, University of Nebraska, Lincoln, NE 68588, USA

⁶Department of Mechanical Engineering and Materials Science, Washington University in St. Louis, St. Louis, MO 63130, USA

*These authors contributed equally: Xin Li, Guodong Ren

✉e-mail: tsybal@unl.edu; agruverman2@unl.edu; rmishra@wustl.edu; xiaoshan.xu@unl.edu

Abstract

The discovery of ferroelectric properties in hafnia-based materials have boosted the potential of incorporating ferroelectricity in advanced electronics, thanks to their compatibility with silicon technology. However, comprehending why these materials defy the common trend of reduced ferroelectric ordering at the nanoscale, and the mechanism that stabilizes the ferroelectric phase—which is absent in hafnia’s phase diagram—presents significant challenges to our traditional knowledge of ferroelectricity. In this work, we show that the formation of the orthorhombic ferroelectric phase (*o-FE*, space group $Pca2_1$) of the single-crystalline epitaxial films of 10% La-doped HfO_2 (LHO) on (111)-oriented yttria stabilized zirconia (YSZ) relies on the stability of the orthorhombic antiferroelectric phase (*o-AFE*, space group $Pbca$) that is present in the high-pressure region of the phase diagram of hafnia. Our detailed x-ray diffraction studies, electron microscopy, and neutron diffraction measurements demonstrate that as-grown LHO films structurally represent an orthorhombic phase that is largely composed of the *o-AFE* phase being thermodynamically stabilized by the compressive strain imposed by the substrate on the lattice of hafnia stretched by La doping. As follows from our Kelvin probe force microscopy studies, under mechanical poling, the *o-AFE* phase is converted to the *o-FE* phase which remains stable under ambient conditions. We find that the orthorhombic phase stability is enhanced with decreasing film thickness down to one unit cell—a trend that is unknown in any other ultrathin ferroelectric films. This is due to the vanishing depolarization field of the *o-AFE* phase and the isomorphic LHO/YSZ interface, supporting strain-enhanced ferroelectricity in the ultrathin films down to the single-unit-cell thickness, as evident from our electron microscopy and reflection high energy electron diffraction studies. This results in an unprecedented increase of the Curie temperature up to 850 °C—the highest reported for sub-nanometer-thick ferroelectrics. Overall, our findings unveil two long-standing mysteries of ferroelectric hafnia—the stability of the *o-FE* phase and its enhancement at the nanoscale, opening the way for advanced engineering of hafnia-based materials for ferroelectric applications and heralding a new frontier of high-temperature ferroelectrics at the two-dimensional limit.

Introduction

Ferroelectric (FE) materials have proven their merits in broad implementations in sensors and actuators. However, integration of traditional perovskite ferroelectrics into modern electronic devices, such as high-density non-volatile memories, has been hindered by their incompatibility with silicon technology and poor scaling behavior. In this regard, hafnia-based ferroelectrics greatly raise the prospect since they have long been used in CMOS-processed electronic devices as high- k dielectric materials and, on top of this, have demonstrated enhancement of their ferroelectric properties at the nanoscale. [1,2]

However, the enhancement of the ferroelectric order at the nanoscale in hafnia-based materials [3,4] is poorly understood. As the thickness of a ferroelectric becomes smaller, depolarization field increases the energy of the ferroelectric state, thereby destabilizing it. This effect reduces the polarization and Curie temperature of both proper and improper ferroelectrics and even completely suppresses ferroelectric order below a certain critical thickness. [5–11] Adding to the puzzle, opposite trends in the thickness dependence of polarization have been reported in hafnia-based films thinner than 10 nm. [12] These discrepancies may be related to uncertainties in polycrystalline and textured epitaxial films and the intricate stabilization mechanisms [13–19] of the ferroelectric orthorhombic phase (o -FE, space group $Pca2_1$, **Fig. 1a**) [20]. In fact, the o -FE phase is absent in hafnia's temperature-pressure phase diagram, which includes, in the order from high to low temperature: cubic (c , space group $Fm\bar{3}m$), tetragonal (t , space group $P4_2/mnc$), and monoclinic (m , space group $P2_1/c$) phases. [21] Additionally, under high pressure, an anti-ferroelectric orthorhombic phase (o -AFE, space group $Pbca$) becomes stable. [21]

The incomplete understanding of the mechanisms that stabilize the o -FE phase and enhance ferroelectric order at the ultrathin limit, is currently hindering the optimization of hafnia's ferroelectric properties for practical applications. To shed light on these mechanisms, growth of single-crystalline thin films and their in-depth atomic scale characterization are needed.

In this work, we discover that single-crystalline $Hf_{0.9}La_{0.1}O_2$ (LHO) films epitaxially grown on (111)-oriented yttria stabilized zirconia (YSZ) can be thermodynamically stabilized under compressive strain in the predominantly o -AFE phase that can be further transformed into the o -FE phase by mechanical poling. These findings suggest that the ferroelectric behavior of hafnia-based thin films hinges on stabilizing the high-pressure o -AFE phase, rather than the commonly assumed t -phase as prerequisite. The vanishing depolarization field in the o -AFE phase and the more effective strain effect in ultrathin films lead to the enhanced orthorhombic structural order, down to the two-dimensional (2D) limit (one unit cell thickness), resulting in an unprecedented 850 °C Curie temperature at the sub-nanometer scale.

Single crystalline films of orthorhombic symmetry

To fabricate single-crystalline LHO films, we opted for yttria stabilized zirconia (YSZ) as the substrate, since YSZ is isomorphic to the c phase of hafnia. Earlier theoretical works suggest that for hafnia films grown along the (111) direction under biaxial compressive strain, the m phase may become less stable than the o -FE and o -AFE phases, [22,23] which we collectively refer as the orthorhombic phases (o phases). This aligns with the approximately 4% reduction of volume per formula unit (v) of the o phases compared to that of the m phase of hafnia [21] (see **Fig. S1**), and with the reports that epitaxial hafnia films grown along the (111) orientation are more likely to form the o phases [24]. However, YSZ is only $\approx 1\%$ smaller than the m phase of pristine hafnia

in terms of the ν value, which is insufficient to thermodynamically stabilize the orthorhombic phases. To increase the ν difference between the m phase hafnia film and the YSZ substrate, we choose the composition $\text{Hf}_{0.9}\text{La}_{0.1}\text{O}_2$, since the large atomic radius of La is expected to expand the hafnia film unit cell. Using density functional theory (DFT) calculations (see details in *Methods* and **Fig. S2**), we studied the stabilization effects of lattice strain imposed on the (111) plane and La-doping theoretically. In agreement with the previous work [22,23], our results show that compressive strain on the (111) plane leads to the stabilization of the o phases (both o -*FE* and o -*AFE*) over the m phase. Moreover, La-doping at 8 at. % concentration causes an expansion of the lattice volume by 3.6% for both o -*FE* and o -*AFE* phases, and 4.0% for the m phase, making the epitaxial strain more effective for stabilizing the o phases, without having to change the substrate. As the epitaxial strain along the (111) plane approaches that imposed by the YSZ substrate, we find the o -*AFE* phase to be most stable in both HfO_2 and $\text{La}_{0.08}\text{Hf}_{0.92}\text{O}_2$. It is followed by the o -*FE* phase, which is only 18 meV/f.u. higher in energy. This implies that the o -*AFE* phase is likely to be the dominant phase when grown epitaxially over YSZ (111) substrates. Additionally, hole-doping due to the La^{3+} ions substituting for Hf^{4+} , has also been proposed to stabilize the o phase over the m phase. [19]

After confirming the ferroelectric behavior in LHO (111)-textured films grown on $\text{La}_{0.7}\text{Sr}_{0.3}\text{MnO}_3 / \text{SrTiO}_3$ (110) (**Fig. S3**) [25], we grow and characterize the structure of LHO films on the (111)-oriented YSZ (see details in **Fig. S4** and **Fig. S5**). The o -*FE* phase features lattice distortions Q_a and Q_b shown in **Fig. 1b,c**, in which Hf atoms displace along the a and b axes, respectively. [26] These distortions lead to single $(010)_o$ and single $(1\bar{1}0)_o$ (subscript “o” indicates the structural coordinates of the o -*FE* phase) diffraction spots that are shown in **Fig. 1d** (see details in **Fig. S6** and **Fig. S7**) for a 21-nm-thick film [26]. The Laue oscillation in the specular $\theta/2\theta$ x-ray diffraction pattern near $(111)_o$ in **Fig. 1e** (**Fig. S8**) indicates a flat film surface and confirms the film thickness. These structural properties are observed for the LHO/YSZ films with the thickness up to at least 30 nm (see **Fig. S6**), which is the largest thickness of ferroelectric hafnia without the m phase reported so far. The lattice constants of the 21.4-nm-thick film are 5.20 ± 0.01 Å for the a axis and 5.11 ± 0.01 Å for the b and c axes (see details in **Fig. S9**). Atomic force microscopy (AFM) images of a 0.65-nm-thick film in **Fig. 1f** show terraces steps of 0.3 nm in height, which correspond to the spacing of the (111) plane of LHO (see details in **Fig. S10**).

We confirm the single-crystalline and single-phase nature of the films from their atomic scale characterization done using an aberration-corrected scanning transmission electron microscope (STEM). A representative high-angle annular dark field (HAADF) image in **Fig. 1g** shows the atomic structure of LHO when viewed along the YSZ $[1\bar{1}0]$ direction (other images with larger field-of-view are shown in **Figs. S11-Fig. S13**). A fast Fourier transform (FFT) of the LHO region (**Fig. 1h**) shows a spot corresponding to the $(010)_o$ plane, and is consistent with the Q_b distortion in **Fig. 1c**. These distortions in LHO further manifest as stripes in the real-space HAADF image in **Fig. 1g**. In contrast, YSZ has a uniform Zr spacing, with no visible stripes. This uniformity is further confirmed by the absence of the spot corresponding to the (010) plane in the FFT pattern shown in **Fig. 1i**. The inhomogeneity of the stripe patterns in the LHO area comes from the three structural twins, which rotate by 120° about the $[111]$ direction of YSZ with respect to each other, as illustrated in **Fig. 1j-l**. The area marked with the red dashed (green dotted) box corresponds to the structure twins in **Fig. 1j** (**Fig. 1k** or **Fig. 1l**). To verify the observed features of the structural twins in LHO, we performed STEM simulations using a DFT-optimized $\text{HfO}_2/\text{ZrO}_2$

supercell structure (see the simulation details in *Methods*). We find excellent agreement between the simulated and the experimental HAADF images (see details in **Fig. S14** and **Fig. S15**).

Notably, even though we use the atomic coordinates of the *o-FE* phase here, all these observations are consistent with both *o-FE* and *o-AFE* phases. As illustrated in **Fig. 2a**, the primary difference between *o-FE* and *o-AFE* phases lies in the oxygen displacements within the polar layers: the unit cell of the *o-AFE* phase is essentially an $1 \times 2 \times 1$ super cell the *o-FE* phase. The two neighboring polar layers in the former have oxygen displacements along opposite directions.

Dominance of the *o-AFE* phase

To elucidate the atomic structure of the orthorhombic LHO films, we studied their polar domain structures using STEM imaging with the film oriented along the LHO $[100]_o$ direction (see STEM observations in **Fig. S16**). An annular bright-field (ABF) STEM image, which has high sensitivity to lighter elements [27], is shown in **Fig. 2b**. It clearly unveils the position of the oxygen columns and is consistent with the simulated ABF images of *o-FE* LHO (see the structural model and the simulated image as insets in **Fig. 2b**). After determining the position of the atomic columns in **Fig. 2b**, the polar distortions (and the domain pattern) can be derived from the offset δ of oxygen columns from the centroid of the four nearest Hf atomic columns.

Fig. 2c shows that the LHO structure consists of stripes of polar regions along the *c* axis (see details in **Fig. S17-S18**). These polar stripes are separated by non-polar spacer stripes. Thickness of the polar and spacer stripes is about half of the lattice constant of the *o-FE* phase. Notice that the direction of the polar displacements in neighboring polar stripes (separated by spacer stripes) are mostly aligned in an antiparallel manner, with a few layers having parallel alignment. Therefore, as seen from **Fig. 2c**, most of the LHO film area represents the *o-AFE* phase. The small regions having parallel oxygen displacements can be viewed as the *o-FE* phase. In fact, the *o-AFE* phase can be considered as a multidomain structure of the *o-FE* phase with one unit cell domain size and infinite number of abrupt domain walls. The antiparallel alignment is expected to quench the depolarization field and the polarization-induced charges at the interface with the YSZ substrate.

The widespread *o-AFE* phase in the sample is further confirmed by neutron diffraction. As the *o-AFE* phase differs from the *o-FE* phase only in the order of the oxygen positions, neutron diffraction is an advantageous probe due to its sensitivity to oxygen. As shown in **Fig. 2d**, substantial intensity was observed around the diffraction peak $(0, \frac{1}{2}, 2)_o$, besides the Al (111) peak from the sample environment. The $\frac{1}{2}$ index is a direct evidence of the unit cell doubling along the *b* axis. This observation confirms the appearance of the *o-AFE* phase over the macroscopic scale of the LHO films.

Converting the *o-AFE* phase to the *o-FE* phase

To understand the relation between the *o-FE* and *o-AFE* phases, we explore the transformation of the *o-AFE* phase into the *o-FE* phase by mechanical poling induced by the AFM tip. **Figs 2e-g** show the Kelvin probe force microscopy (KPFM) images of the LHO films of different thickness after their central regions of $1 \mu\text{m} \times 1 \mu\text{m}$ were mechanically poled by scanning with the tip under a high loading force of 1500 nN. (See **Fig. S20** for the force dependence of the KPFM signal). An increase of the KPFM signal in the regions subjected to mechanical pressure is an indication of polarization generated by the tip-induced strain gradient via the flexoelectric effect [28].

We define ΔV as average surface potential related to the background. As shown in **Fig. 2h**, for the 0.3 nm LHO film, $\Delta V \approx 0.09$ V, which jumps to $\Delta V \approx 0.26$ V for the 0.6 nm film. For the 1.4 nm film, ΔV is reduced to 0.17 V. Therefore, mechanical poling appears to be able to convert the *o-AFE* phase with the minimal net polarization into the *o-FE* phase with finite remanent polarization.

Orthorhombic structure of the interfacial unit cell

To understand the enhanced ferroelectric order of hafnia at the ultrathin limit, we delve into the interfacial structures of the LHO films. **Fig. 3a** displays a HAADF image of a 10-nm-thick LHO film viewed along the $[11\bar{2}]$ direction of YSZ. A dimerization pattern due to the pairing of Hf atoms along the horizontal direction, which is caused by the Q_a and Q_b distortion modes illustrated in **Fig. 1b,c**, is visible. A close-up view of the interfacial area in the yellow dashed box is shown in **Fig. 3b** (see chemical information near the interface in **Fig. S19**). As indicated in the atomic structure model in **Fig. 3c**, the horizontal distance between Hf atoms splits into two values x_{short} and x_{long} which are visible when the structure is viewed along the $[11\bar{2}]_o$ direction. In addition, Hf atoms on the $(111)_o$ plane displace vertically, as described by Δy .

Quantitative description of the distortions can be obtained by calculating $\Delta x = x_{\text{long}} - x_{\text{short}}$, and Δy from the STEM image. The results are displayed in **Fig. 3d**, where the index of the topmost YSZ monolayer is 0. In YSZ, far away from the interface, both Δx and Δy values are approximately zero, as expected from the cubic structure of YSZ. In contrast, in LHO, far away from the interface, Δx and Δy are approximately 0.6 and 0.15 Å, respectively. On the LHO side close to the interface, Δx and Δy reach their ultimate value in the first unit cell thickness (2 monolayers, 0.6 nm). Interestingly, on the YSZ side, non-zero distortions are observed in the top two monolayers, as indicated in **Fig. 3d** and visible in **Fig. 3b**. In other words, while YSZ barely reduces the distortion in LHO, LHO induces the orthorhombic distortion in the top two monolayers (one unit cell) of YSZ, corresponding to ferroelectric proximity effect at FE/non-FE interface [29,30]. These features are in stark contrast to the distortions observed in perovskite-structure ferroelectrics, wherein the substrate suppresses the distortions in the film at the interface, while undergoing minimal distortions itself. [31,32]

To further understand the distortion at the LHO/YSZ interface, we performed DFT calculations, as described in *Methods*. As shown in **Fig. 3e**, we considered a heterostructure where five-monolayer HfO₂ (111) was deposited on ZrO₂ (111) substrate with polarization of the HfO₂ layers pointing to or away from the interface. After performing the structural relaxation, we found that all HfO₂ monolayers including those close to the interface exhibit nearly the same structural distortions as those in the bulk orthorhombic HfO₂. At the same time, we observed that these distortions propagate into the first two monolayers of ZrO₂ near the interface. Since the experimentally dominated *o-AFE* phase essentially represents an $1 \times 2 \times 1$ super cell of the *o-FE* phase, we averaged the calculated distortions Δx and Δy over the two polarization orientations of the *o-FE* phase. The calculated distortions appear to be in excellent agreement with our experiments, as shown in **Fig. 3d** (see **Fig. S21** and **Fig. S22** for the calculated oxygen displacements).

Record-high Curie temperature in the 2D limit

The orthorhombic structure of the LHO films in the 2D limit was studied using reflection high energy electron diffraction (RHEED). **Fig. 4a** shows the RHEED images of the YSZ substrate and the LHO film of different thickness, with electron beam along the YSZ $[1\bar{1}0]$ direction,

measured at room temperature, where the diffraction lines are labeled according to the YSZ coordinates (c phase). Besides the specular reflection in the middle, YSZ shows only the $(22\bar{4})$ and $(\bar{2}\bar{2}4)$ diffraction peaks, consistent with its face-center-cubic structure in which diffraction is only allowed when the Miller indices are all odd or all even. Below 0.5 nm, the LHO film shows fractional diffraction streaks $\pm n/3$ ($22\bar{4}$), where n is integer. This pattern is consistent with a monolayer structure of the LHO (111) plane (see more details in **Fig. S23 - Fig. S25**), where there is no translational symmetry along the out-of-plane direction. When the film thickness reaches two monolayers (0.6 nm) of the LHO (111) plane or one unit cell, the fractional diffraction streaks disappear, due to the interference caused by the two layers.

As shown in **Fig. 4b**, with electron beam incident along the YSZ $[11\bar{2}]$ direction, the $\pm(1\bar{1}0)$ and $\pm(3\bar{3}0)$ streaks, which are not allowed in the t phase, are discernable at 0.3 nm thickness and increase rapidly at 0.6 nm. The jump of the $(3\bar{3}0)$ peak intensity is more obvious in **Fig. 4c** where the spectra are normalized using the $(4\bar{4}0)$ peak which is allowed in the t phase. We then use the intensity ratio $I_{(3\bar{3}0)}/I_{(4\bar{4}0)}$ as the order parameter for the o phase [33,34], and plot the thickness dependence in a wider range in **Fig. 4d**. The order parameter $I_{(3\bar{3}0)}/I_{(4\bar{4}0)}$ has a clear jump between 0.5 nm and 0.6 nm, when LHO reaches one-unit-cell thickness. As the thickness further increases, $I_{(3\bar{3}0)}/I_{(4\bar{4}0)}$ decreases. Therefore, LHO films adopt the o phase structure in its 2D limit or one-unit-cell thickness, consistent with the STEM results in **Fig. 3d**, suggesting absence of critical thickness. The thickness dependence of order parameter is consistent with that of ΔV in **Fig. 2h**, suggesting that that ΔV is related to the polar order in LHO.

The stronger orthorhombic order at ultrathin limit is confirmed by the temperature dependence of the order parameter $I_{(3\bar{3}0)}/I_{(4\bar{4}0)}$. As shown in **Fig. 4e**, $I_{(3\bar{3}0)}/I_{(4\bar{4}0)}$ decreases with temperature, suggesting that the o phase approaches the t phase at high temperature, corresponding to the structural phase transition. For thinner (0.6 and 0.8 nm) films, the transition appears to occur at Curie temperature $T_C = 850 \pm 50$ °C. For thicker (8.0 and 9.0 nm) films, the transition occurs at a lower $T_C = 600 \pm 50$ °C, which is closer to the T_C reported previously in Y-doped hafnia films of similar thickness [26,34,35].

Figure 3f compares the thickness dependence of transition temperature of various ferroelectrics. [5,10,11,36–42] Single-crystalline LHO stands out in that the T_C increases in thinner films, reaching a record-high value of 850 °C in the 2D limit.

Discussion

We demonstrate that the LHO / YSZ (111) films are stabilized in the o phases by compressive epitaxial strain, which is supported by three observations. First, for LHO films thinner than 1 nm (**Fig. 4e**), the growth temperature (750 °C) remains below T_C , indicating thermodynamic stability of the o phases. Consequently, kinetic stabilization through the t phase is not necessary [34,43] (**Fig. S1b**). Second, the enhanced T_C at the ultrathin limit (**Fig. 3f**) suggests that the o phases become more stable in thinner films, where epitaxial strain is more effective [44]. Third, we conducted epitaxial growth of an additional series of thin films of $\text{Hf}_{0.5}\text{Zr}_{0.5}\text{O}_2$ (HZO), $\text{Hf}_{0.68}\text{Zr}_{0.32}\text{O}_2$ (HZO32), and $\text{Hf}_{0.95}\text{Y}_{0.05}\text{O}_2$ (YHO) on YSZ (111). Interestingly, we observed a 3D island growth mode for those films, unlike the 2D-film growth mode of LHO (**Fig. S26**). The 3D growth mode indicates high interfacial energy. Notably, the lattice constants of HZO, HZO32, and YHO are smaller than that of LHO (**Fig. S27**), corresponding to smaller strains. The intriguing combination of larger strain but smaller interfacial energy in LHO/YSZ films compared with that

of YHO, HZO, and HZO32, suggests that LHO/YSZ achieves a stable state of the *o* phases under the compressive strain.

The stabilization of the *o-FE* phase depends on the stability of the *o-AFE* phase. The remanent polarization arises due to the small energy difference and high energy barrier between the *o-FE* and *o-AFE* phases. [45,46] Specifically, according to ref. [47], the energy difference between the *o-FE* and *o-AFE* phases of HfO₂ is about 0.08 eV per unit cell while the energy barrier for the switching is about 0.52 eV. Therefore, when hafnia is converted from the *o-AFE* phase to the *o-FE* phase, either by electric-field poling [47] or by mechanical poling (**Fig. 2e-h**), the high energy barrier keeps the *o-FE* phase from reverting back to the *o-AFE* phase, even though the latter has slightly lower energy.

Finally, it is important to note that the enhanced ferroelectric order in ultrathin films relies on structural matching between the film and the substrate at the interface. It is known that interfacial reconstruction and bonding between a non-polar substrate and a polar film tends to reduce the polar distortion of the film at the interface. [9–11,31,32] In particular, reconstruction in hafnia can induce the *t* phase at the interface [48], reducing the Curie temperature at smaller thickness [44]. However, for the LHO/YSZ (111) heterostructure, the structural matching at the interface allows LHO to even induce the polar distortion in the top monolayers of YSZ, which is essential for the enhanced ferroelectric order at the 2D limit.

Conclusion and outlook

This work resolves the long-standing mysteries of stabilization mechanisms of the ferroelectric phase of hafnia and enhancement of ferroelectric order at the nanoscale. The key is that the stable *o-FE* phase is obtained by poling the high-pressure *o-AFE* phase which is stabilized by compressive strain. The minimized depolarization field in LHO due to the dominance of the *o-AFE* phase during the film growth and a more effective strain effect in the ultrathin limit lead to the enhanced orthorhombic order and significantly increased Curie temperature (up to 850 ± 50 °C) in one-unit-cell thick LHO films. These elucidations are essential to overcome the challenge of hafnia to conventional understanding of ferroelectricity and are expected to speed up the process of engineering hafnia for ferroelectric applications especially in the 2D limit.

Experimental Methods

Sample preparation

The LHO thin films on yttria stabilized zirconia (YSZ) substrate were grown by pulsed laser deposition (PLD) with a wavelength of 248 nm. The base pressure of the PLD chamber is around 3×10^{-7} mTorr. Before the deposition, the YSZ substrates were pre-annealed at 900 °C for 1 h in the PLD chamber. The growth temperature is fixed at 750 °C (measured by an external pyrometer) for optimal growth, with a repetition rate of 2 Hz and an oxygen pressure of 70 mTorr. At the end of the deposition, the temperature of the films was decreased to room temperature with a cooling rate of 20 °C/min under the oxygen pressure of 70 mTorr. Substrate temperature was measured using an external pyrometer.

X-ray structural characterization

The structural characterizations, including specular x-ray θ - 2θ scans, and x-ray reflectivity, were performed by a Rigaku SmartLab diffractometer using Cu K α radiation (wavelength, 1.54 Å). The non-specular {010} and {1-10} planes in the LHO films were measured using a Bruker AXS D8 Discover diffractometer with an area detector with x-ray wavelength 1.54 Å.

Neutron diffraction

Single-crystal neutron diffraction experiments were carried out at the beam line HB-3A DEMAND [49] at the High Flux Reactor (HFIR) with a thermal neutron wavelength of 1.533 Å, in the Oak Ridge National Laboratory. The aluminum pin was used to hold the film sample and the measurement was performed at ambient temperature of 295 K.

In-situ RHEED measurement and analysis

The reflection high energy electron diffraction (RHEED) images were captured with 20 kV electron beam. For thickness dependence measurements, the images were captured continuously during growth with fixed temperature. For temperature dependence measurements, the images were captured after the film growth, by varying the substrate temperature. The diffraction intensity and peak position of individual peaks are extracted and quantified from the raw RHEED images using Gaussian fitting.

Electrical measurements

For the measurements of the ferroelectric properties for LHO/LSMO/STO(110) film at room temperature, a solid Pt tip (RMN-25PT400B, Rocky Mountain Nanotechnology) in contact with the Pt top electrode was used to apply the voltage pulses using a Keysight 33621A arbitrary waveform generator, whereas the transient switching currents through the bottom electrode were recorded by a Tektronix TDS 3014B oscilloscope. In all the measurements, the bias was applied to the top electrode (diameter ranging from 75 to 400 μ m), whereas the LSMO bottom electrode was grounded.

Scanning probe microscopy

The atomic force microscopy (AFM) images were obtained with a Bruker Dimension Icon Atomic Force Microscope, using silicon nitride probes in the scan-analysis air mode. The Kelvin probe force microscopy measurements were carried out using the Asylum Research AFM system (MFP-3D) in a double-pass lift-off (50 nm) mode. The Pt-coated Si probes (PPP-EFM, Nanosensors) were used for the surface potential imaging. Mechanical poling was performed by

scanning the sample surface in the contact mode with the tip under a high constant mechanical load of up to 1500 nN. The spring constant of the cantilevers was calibrated by the built-in thermo noise method.

Electron microscopy

Three TEM lamellae along different orientations were prepared from the same LHO thin film using a ThermoFisher Scios 2 DualBeam FIB including a polishing process at 2 KeV. All TEM lamellae were further thinned down to an electron-transparent thickness utilizing a Fischione’s Model 1040 NanoMill TEM specimen preparation system at an operating voltage of 900 V.

Atomic resolution Z -contrast HAADF-STEM imaging was carried out on Nion UltraSTEMTM 100 and 200 microscopes, both equipped with a spherical aberration corrector, operating at 100 kV and 200 kV, respectively. The HAADF images were acquired with a convergence semi-angle of 30 mrad and collection semi-angles from 80 to 200 mrad. To resolve the position of oxygen columns, we have also conducted annular bright-field (ABF) imaging with a collection semi-angle of 15~30 mrad.

STEM simulations to compare with experimental data were performed using the multi-slice method as implemented in μ STEM [50]. A 17-layer heterostructure including seven layers of cubic ZrO₂ sandwiched by five layers of o -FE HfO₂ with ferroelectric order optimized by DFT (described below) were used for the STEM simulations. To match the experimental conditions, we performed the simulations using an aberration-free probe with an accelerating voltage of 100 kV and a convergence semiangle of 30 mrad. Thermal scattering was included through the phonon excitation model proposed by Forbes et al [51]. The sample thickness was set to 15 nm and the defocus value was set to 10 Å to obtain good agreement with the experimental data.

4D-STEM experiments were carried out on Nion UltraSTEMTM at 100 kV using a Dectris ELA high-speed electron-counting detector. Differential phase contrast (STEM-DPC) datasets were acquired with 256×256 pixels using a 30 mrad convergent beam. The core-loss electron energy loss spectra (EELS) were acquired with pixel dwell times of 3 ms, energy dispersion of 1 eV per channel, and a collection semi-angle of 35 mrad on a Nion Iris spectrometer attached to the Nion UltraSTEMTM. The spectrum images were processed using the Digital Micrograph software.

DFT calculations

The electronic structure and structural optimization calculations were carried out based on density functional theory (DFT) using the plane-wave projected augmented wave (PAW) method as implemented in Vienna Ab-initio Simulation Package (VASP) [52–54]. To investigate the phase stabilization from lattice strain on (111) plane and La-doping effects, we converted the unit cell of o -FE phase, o -AFE phase, and m phase into pseudo-hexagonal lattice with (111) plane as base plane (see converted lattice in **Fig. S30**). The converted lattices were optimized under epitaxial strain within (111) plane, while atomic positions are free to relax out of (111) plane. The total energy of optimized lattices was compared with the unstrained ground-state m phase. Special quasirandom structure (SQS) method [55] was applied to creating optimal solid solution lattice of LHO phase with 8 at.% La doping concentration. In these calculations, a plane-wave basis with an energy cutoff of 600 eV has been applied. The Brillouin zone was sampled using a Γ -centered k -point mesh with spacing of 0.035 \AA^{-1} for the o -FE, the o -AFE and the m phases. The crystal structures were optimized until all forces on the atoms were less than 0.01 eV/\AA .

To investigate the interface structure, [57] a HfO₂/ZrO₂/HfO₂ (111) supercell was constructed, consisting of five-monolayer HfO₂ (111) on either side of seven-monolayer ZrO₂ (111). Bulk orthorhombic HfO₂ of the space group Pca2₁ and bulk cubic ZrO₂ of the space group Fm-3m were used to build the supercell. The in-plane lattice constants of the (111) supercell were fixed to $a = b = 7.24077$ Å consistent with the lattice parameters of the bulk Y-doped ZrO₂ (001) ($a = b = c = 5.120$ Å). Both the HfO₂ (111) layers had electric polarization pointing to the [001] direction, which implied that the polarization of the top layer was pointing away from the HfO₂/ZrO₂ interface, while the polarization of the bottom HfO₂ layer was pointing to the HfO₂/ZrO₂ interface. A 21 Å vacuum layer was included in the supercell to minimize the interaction between the periodically repeated slabs along the z-axis. **Fig. 3e** shows the atomic structure of the supercell split into the top and bottom parts. The atomic positions were relaxed toward equilibrium until the Hellman–Feynman forces became less than 0.01 eV/Å. During the optimization, the middle monolayer of ZrO₂ was kept fixed to impose the boundary conduction of bulk ZrO₂. A plane-wave cutoff of 480 eV and a k -point mesh of $6 \times 6 \times 1$ was used for the structural optimization of the heterostructure.

Acknowledgements

This work was primarily supported by the Intel Corporation (X.L, A.S., H.L, X.X., and A.G.). R.M., G.R., and P.O. acknowledge the National Science Foundation (NSF) of the United States under grant numbers DMR-2122070 and DMR-2145797. M.C. A. R. L. and J. A. H. are supported by the U.S. Department of Energy, Office of Science, Basic Energy Sciences, Materials Sciences and Engineering Division. The Microscopy work was conducted as part of a user project at the Center for Nanophase Materials Sciences (CNMS), which is a US Department of Energy, Office of Science User Facility at Oak Ridge National Laboratory. This work used computational resources through allocation DMR160007 from the Advanced Cyberinfrastructure Coordination Ecosystem: Services & Support (ACCESS) program, which is supported by NSF grants #2138259, #2138286, #2138307, #2137603, and #2138296. This research used resources at the High Flux Isotope Reactor, a DOE Office of Science User Facility operated by the Oak Ridge National Laboratory. [The beam time was allocated to DEMAND on proposal number IPTS-33539.1.] The research was performed in part in the Nebraska Nanoscale Facility: National Nanotechnology Coordinated Infrastructure and the Nebraska Center for Materials and Nanoscience (and/or NERCF), which are supported by the National Science Foundation under Award ECCS: 2025298, and the Nebraska Research Initiative. We acknowledge Dr. Huafang Li and Jian Huang of Washington University for help with TEM specimen preparation.

Author contributions

The thin film synthesis and x-ray diffractions were carried out by A.S. X.L., and Y.Y. under the supervision of X.X. Thickness-resolved RHEED was measured and analyzed by X.L. and X.X. KPFM was studied and analyzed by H.L. under the supervision of A.G. Electric polarization switching were studied and analyzed by P.B. under the supervision of A.G. DFT calculations were conducted by K.S., P.O., and G.R. under the supervision of E.Y.T. and R.M. (S)TEM experiments were conducted by G.R. under the supervision of R.M., A.R.L., J.A.H, and M.C. The study was conceived by X.L. and X.X. X.L., G.R., H.L, R.M, E.Y.T., A.G., and X.X. co-wrote the manuscript. All the authors discussed the results and commented on the manuscript.

Competing interests

The authors declare no competing interests.

References

- [1] J. P. B. Silva et al., *Roadmap on Ferroelectric Hafnia- and Zirconia-Based Materials and Devices*, APL Mater **11**, 089201 (2023).
- [2] J. Cao, S. Shi, Y. Zhu, and J. Chen, *An Overview of Ferroelectric Hafnia and Epitaxial Growth*, Physica Status Solidi (RRL) – Rapid Research Letters **15**, 2100025 (2021).
- [3] M. Hyuk Park, H. Joon Kim, Y. Jin Kim, W. Lee, T. Moon, and C. Seong Hwang, *Evolution of Phases and Ferroelectric Properties of Thin Hf_{0.5}Zr_{0.5}O₂ Films According to the Thickness and Annealing Temperature*, Appl Phys Lett **102**, (2013).
- [4] S. S. Cheema et al., *Enhanced Ferroelectricity in Ultrathin Films Grown Directly on Silicon*, Nature **580**, 478 (2020).
- [5] D. D. Fong, G. B. Stephenson, S. K. Streiffer, J. A. Eastman, O. Auciello, P. H. Fuoss, and C. Thompson, *Ferroelectricity in Ultrathin Perovskite Films.*, Science **304**, 1650 (2004).
- [6] Y. S. Kim et al., *Critical Thickness of Ultrathin Ferroelectric BaTiO₃ Films*, Appl Phys Lett **86**, 102907 (2005).
- [7] Javier Junquera and P. Ghosez, *Critical Thickness for Ferroelectricity in Perovskite Ultrathin Film*, Nature **422**, 506 (2003).
- [8] J. E. Rault, W. Ren, S. Prosandeev, S. Lisenkov, D. Sando, S. Fusil, M. Bibes, A. Barthélémy, L. Bellaïche, and N. Barrett, *Thickness-Dependent Polarization of Strained BiFeO₃ Films with Constant Tetragonality*, Phys Rev Lett **109**, 267601 (2012).
- [9] Y. Yun, P. Buragohain, A. S. Thind, Y. Yin, X. Li, X. Jiang, R. Mishra, A. Gruverman, and X. Xu, *Spontaneous Polarization in an Ultrathin Improper-Ferroelectric/Dielectric Bilayer in a Capacitor Structure at Cryogenic Temperatures*, Phys Rev Appl **18**, 34071 (2022).
- [10] X. Li, Y. Yun, and X. Xu, *Improper Ferroelectricity in Ultrathin Hexagonal Ferrites Films*, Appl Phys Lett **122**, 182901 (2023).
- [11] J. Nordlander, M. Campanini, M. D. Rossell, R. Erni, Q. N. Meier, A. Cano, N. A. Spaldin, M. Fiebig, and M. Trassin, *The Ultrathin Limit of Improper Ferroelectricity*, Nat Commun **10**, 5591 (2019).
- [12] J. Lyu, T. Song, I. Fina, and F. Sánchez, *High Polarization, Endurance and Retention in Sub-5 Nm Hf_{0.5}Zr_{0.5}O₂films*, Nanoscale **12**, 11280 (2020).

- [13] R. Batra, H. D. Tran, and R. Ramprasad, *Stabilization of Metastable Phases in Hafnia Owing to Surface Energy Effects*, Appl Phys Lett **108**, (2016).
- [14] R. Materlik, C. Künneth, and A. Kersch, *The Origin of Ferroelectricity in $Hf_{1-x}Zr_xO_2$: A Computational Investigation and a Surface Energy Model*, J Appl Phys **117**, 134109 (2015).
- [15] M. H. Park, Y. H. Lee, H. J. Kim, Y. J. Kim, T. Moon, K. Do Kim, S. D. Hyun, T. Mikolajick, U. Schroeder, and C. S. Hwang, *Understanding the Formation of the Metastable Ferroelectric Phase in Hafnia-Zirconia Solid Solution Thin Films*, Nanoscale **10**, 716 (2018).
- [16] M. H. Park, Y. H. Lee, H. J. Kim, T. Schenk, W. Lee, K. Do Kim, F. P. G. Fengler, T. Mikolajick, U. Schroeder, and C. S. Hwang, *Surface and Grain Boundary Energy as the Key Enabler of Ferroelectricity in Nanoscale Hafnia-Zirconia: A Comparison of Model and Experiment*, Nanoscale **9**, 9973 (2017).
- [17] X. Xu, F. T. Huang, Y. Qi, S. Singh, K. M. Rabe, D. Obeysekera, J. Yang, M. W. Chu, and S. W. Cheong, *Kinetically Stabilized Ferroelectricity in Bulk Single-Crystalline $HfO_2:Y$* , Nat Mater **20**, 826 (2021).
- [18] J. Lyu, I. Fina, R. Solanas, J. Fontcuberta, and F. Sanchez, *Growth Window of Ferroelectric Epitaxial $Hf_{0.5}Zr_{0.5}O_2$ Thin Films*, ACS Appl Electron Mater **1**, 220 (2019).
- [19] T. Cao, G. Ren, D.-F. Shao, E. Y. Tsybal, and R. Mishra, *Stabilizing Polar Phases in Binary Metal Oxides by Hole Doping*, Phys Rev Mater **7**, 44412 (2023).
- [20] R. Materlik, C. Künneth, and A. Kersch, *The Origin of Ferroelectricity in $Hf_{1-x}Zr_xO_2$: A Computational Investigation and a Surface Energy Model*, J Appl Phys **117**, (2015).
- [21] O. Ohtaka, H. Fukui, T. Kunisada, T. Fujisawa, K. Funakoshi, W. Utsumi, T. Irifune, K. Kuroda, and T. Kikegawa, *Phase Relations and Volume Changes of Hafnia under High Pressure and High Temperature*, Journal of the American Ceramic Society **84**, 1369 (2001).
- [22] S. Liu and B. M. Hanrahan, *Effects of Growth Orientations and Epitaxial Strains on Phase Stability of HfO_2 Thin Films*, Phys Rev Mater **3**, 054404 (2019).
- [23] T. Zhu, S. Deng, and S. Liu, *Epitaxial Ferroelectric Hafnia Stabilized by Symmetry Constraints*, Phys Rev B **108**, L060102 (2023).
- [24] E. Barriuso, R. Jiménez, E. Langenberg, P. Koutsogiannis, Á. Larrea, M. Varela, C. Magén, P. A. Algarabel, M. Alguero, and J. A. Pardo, *Epitaxy-Driven Ferroelectric/Non-*

- Ferroelectric Polymorph Selection in an All-Fluorite System*, Adv Electron Mater **10**, 2300522 (2024).
- [25] T. Song, H. Tan, R. Bachelet, G. Saint-Girons, I. Fina, and F. Sánchez, *Impact of La Concentration on Ferroelectricity of La-Doped HfO₂ Epitaxial Thin Films*, ACS Appl Electron Mater **3**, 4809 (2021).
- [26] Y. Yun et al., *Intrinsic Ferroelectricity in Y-Doped HfO₂ Thin Films.*, Nat Mater **21**, 903 (2022).
- [27] R. Ishikawa, E. Okunishi, H. Sawada, Y. Kondo, F. Hosokawa, and E. Abe, *Direct Imaging of Hydrogen-Atom Columns in a Crystal by Annular Bright-Field Electron Microscopy*, Nat Mater **10**, 278 (2011).
- [28] H. Lu, C. W. Bark, D. Esque De Los Ojos, J. Alcala, C. B. Eom, G. Catalan, and A. Gruverman, *Mechanical Writing of Ferroelectric Polarization*, Science (1979) **335**, 59 (2012).
- [29] L. Wang et al., *Ferroelectrically Tunable Magnetic Skyrmions in Ultrathin Oxide Heterostructures*, Nat Mater **17**, 1087 (2018).
- [30] M. F. Chisholm, W. Luo, M. P. Oxley, S. T. Pantelides, and H. N. Lee, *Atomic-Scale Compensation Phenomena at Polar Interfaces*, Phys Rev Lett **105**, 197602 (2010).
- [31] Y. M. Kim, A. Morozovska, E. Eliseev, M. P. Oxley, R. Mishra, S. M. Selbach, T. Grande, S. T. Pantelides, S. V. Kalinin, and A. Y. Borisevich, *Direct Observation of Ferroelectric Field Effect and Vacancy-Controlled Screening at the BiFeO₃/La_xSr_{1-x}MnO₃ interface*, Nat Mater **13**, 1019 (2014).
- [32] J. Gazquez, M. Stengel, R. Mishra, M. Scigaj, M. Varela, M. A. Roldan, J. Fontcuberta, F. Sánchez, and G. Herranz, *Competition between Polar and Nonpolar Lattice Distortions in Oxide Quantum Wells: New Critical Thickness at Polar Interfaces*, Phys Rev Lett **119**, 106102 (2017).
- [33] T. Mimura, T. Shimizu, T. Kiguchi, A. Akama, T. J. Konno, Y. Katsuya, O. Sakata, and H. Funakubo, *Effects of Heat Treatment and in Situ High-Temperature X-Ray Diffraction Study on the Formation of Ferroelectric Epitaxial Y-Doped HfO₂ Film*, Jpn J Appl Phys **58**, SBBB09 (2019).
- [34] Y. Tashiro, T. Shimizu, T. Mimura, and H. Funakubo, *Comprehensive Study on the Kinetic Formation of the Orthorhombic Ferroelectric Phase in Epitaxial Y-Doped Ferroelectric HfO₂ Thin Films*, ACS Appl Electron Mater **3**, 3123 (2021).

- [35] T. Shimizu, K. Katayama, T. Kiguchi, A. Akama, T. J. Konno, and H. Funakubo, *Growth of Epitaxial Orthorhombic YO_{1.5}-Substituted HfO₂ Thin Film*, Appl Phys Lett **107**, (2015).
- [36] D. A. Tenne et al., *Ferroelectricity in Ultrathin BaTiO₃ Films: Probing the Size Effect by Ultraviolet Raman Spectroscopy*, Phys Rev Lett **103**, 177601 (2009).
- [37] A. V. Bune, V. M. Fridkin, S. Ducharme, L. M. Blinov, S. P. Palto, A. V. Sorokin, S. G. Yudin, and A. Ziatkin, *Two-Dimensional Ferroelectric Films*, Nature **391**, 874 (1998).
- [38] C. Kai et al., *Discovery of Robust In-Plane Ferroelectricity in Atomic-Thick SnTe*, Science (1979) **353**, 274 (2016).
- [39] Q. Song et al., *Evidence for a Single-Layer van Der Waals Multiferroic*, Nature **602**, 601 (2022).
- [40] C. Wang, L. You, D. Cobden, and J. Wang, *Towards Two-Dimensional van Der Waals Ferroelectrics*, Nat Mater **22**, 542 (2023).
- [41] Z. Fei, W. Zhao, T. A. Palomaki, B. Sun, M. K. Miller, Z. Zhao, J. Yan, X. Xu, and D. H. Cobden, *Ferroelectric Switching of a Two-Dimensional Metal*, Nature **560**, 336 (2018).
- [42] J. Xiao et al., *Intrinsic Two-Dimensional Ferroelectricity with Dipole Locking*, Phys Rev Lett **120**, 227601 (2018).
- [43] T. Mikolajick and U. Schroeder, *Ferroelectricity in Bulk Hafnia*, Nat Mater **20**, 718 (2021).
- [44] T. Mimura, T. Shimizu, Y. Katsuya, O. Sakata, and H. Funakubo, *Thickness- and Orientation- Dependences of Curie Temperature in Ferroelectric Epitaxial Y Doped HfO₂ Films*, Jpn J Appl Phys **59**, SGGB04 (2020).
- [45] H.-J. Lee, M. Lee, K. Lee, J. Jo, H. Yang, Y. Kim, S. Chul Chae, U. Waghmare, and J. H. Lee, *Scale-Free Ferroelectricity Induced by Flat Phonon Bands in HfO₂*, Science **369**, 1343 (2020).
- [46] Y. Wu, Y. Zhang, J. Jiang, L. Jiang, M. Tang, Y. Zhou, M. Liao, Q. Yang, and E. Y. Tsymlal, *Unconventional Polarization-Switching Mechanism in (Hf, Zr)O₂. Ferroelectrics and Its Implications*, Phys Rev Lett **131**, 226802 (2023).
- [47] Y. Cheng et al., *Reversible Transition between the Polar and Antipolar Phases and Its Implications for Wake-up and Fatigue in HfO₂-Based Ferroelectric Thin Film*, Nat Commun **13**, 645 (2022).

- [48] Y. Wei et al., *A Rhombohedral Ferroelectric Phase in Epitaxially Strained Hf_{0.5}Zr_{0.5}O₂ Thin Films*, *Nat Mater* **17**, 1095 (2018).
- [49] H. Cao et al., *DEMAND, a Dimensional Extreme Magnetic Neutron Diffractometer at the High Flux Isotope Reactor*, *Crystals (Basel)* **9**, 5 (2018).
- [50] L. J. Allen, A. J. D'Alfonso, and S. D. Findlay, *Modelling the Inelastic Scattering of Fast Electrons*, *Ultramicroscopy* **151**, 11 (2015).
- [51] B. D. Forbes, A. V Martin, S. D. Findlay, A. J. D'Alfonso, and L. J. Allen, *Quantum Mechanical Model for Phonon Excitation in Electron Diffraction and Imaging Using a Born-Oppenheimer Approximation*, *Phys Rev B* **82**, 104103 (2010).
- [52] G. Kresse and J. Furthmüller, *Efficient Iterative Schemes for Ab Initio Total-Energy Calculations Using a Plane-Wave Basis Set*, *Phys Rev B* **54**, 11169 (1996).
- [53] G. Kresse and D. Joubert, *From Ultrasoft Pseudopotentials to the Projector Augmented-Wave Method*, *Phys Rev B* **59**, 1758 (1999).
- [54] P. E. Blöchl, *Projector Augmented-Wave Method*, *Phys Rev B* **50**, 17953 (1994).
- [55] A. Zunger, S.-H. Wei, L. G. Ferreira, and J. E. Bernard, *Special Quasirandom Structures*, *Phys Rev Lett* **65**, 353 (1990).

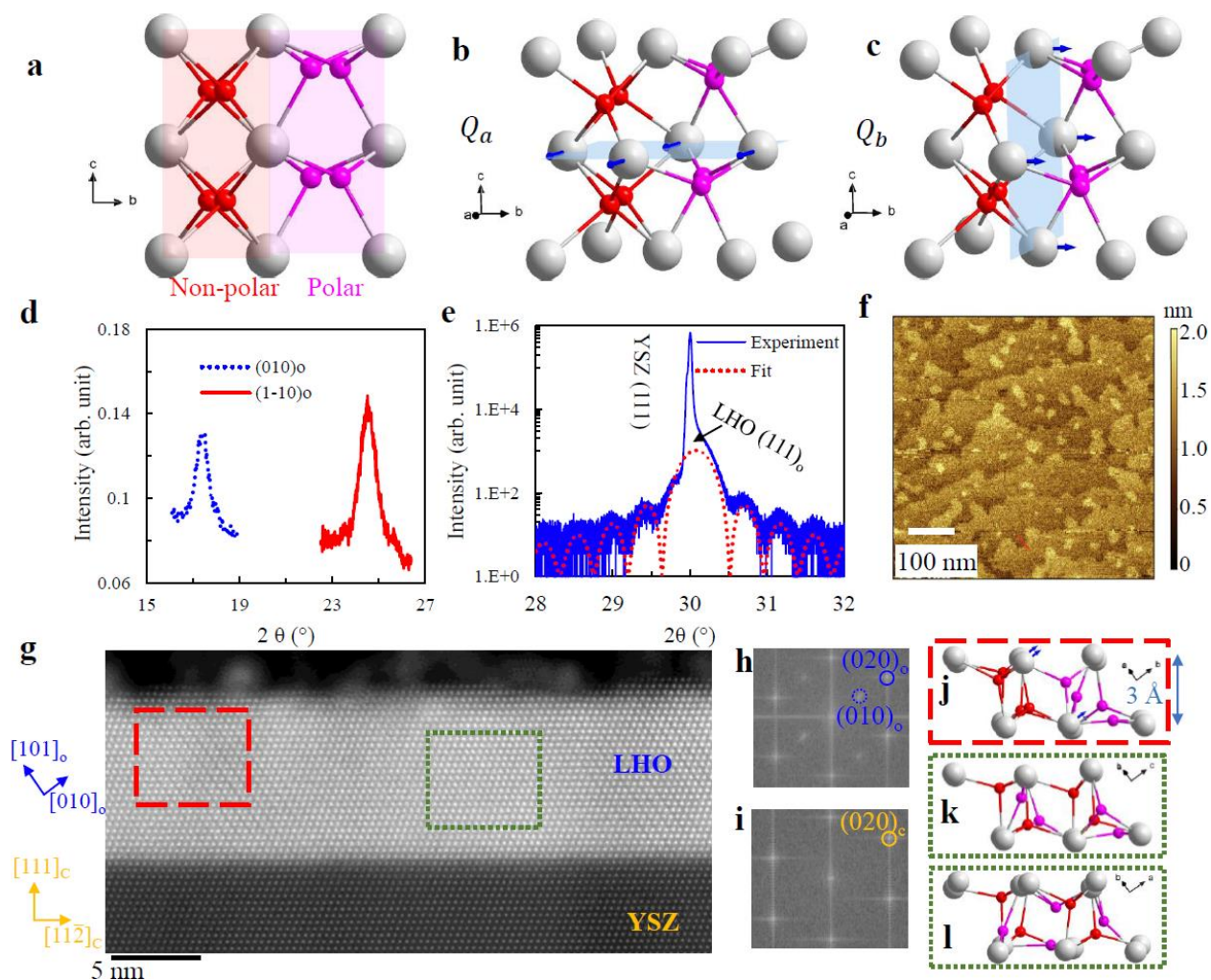


Figure 1. Single-crystalline epitaxial LHO (111) / YSZ (111) films. (a) Crystal structure of the *o*-FE ($Pca2_1$) phase of hafnia. (b) and (c) are the two structural distortions of the *o*-FE phases in terms of the Hf displacement. (d) and (e) are the non-specular and specular x-ray diffractions of a 21.4-nm LHO film respectively. (f) AFM images of a 0.65-nm film showing atomic terraces. (g) A representative HAADF-STEM image viewed from the YSZ $[1\bar{1}0]$ direction. (h) and (i) are Fourier transforms of the LHO (top) and YSZ (bottom) respectively. (j-l) are unit cells of LHO (111) viewed along different directions, corresponding to three structural twins.

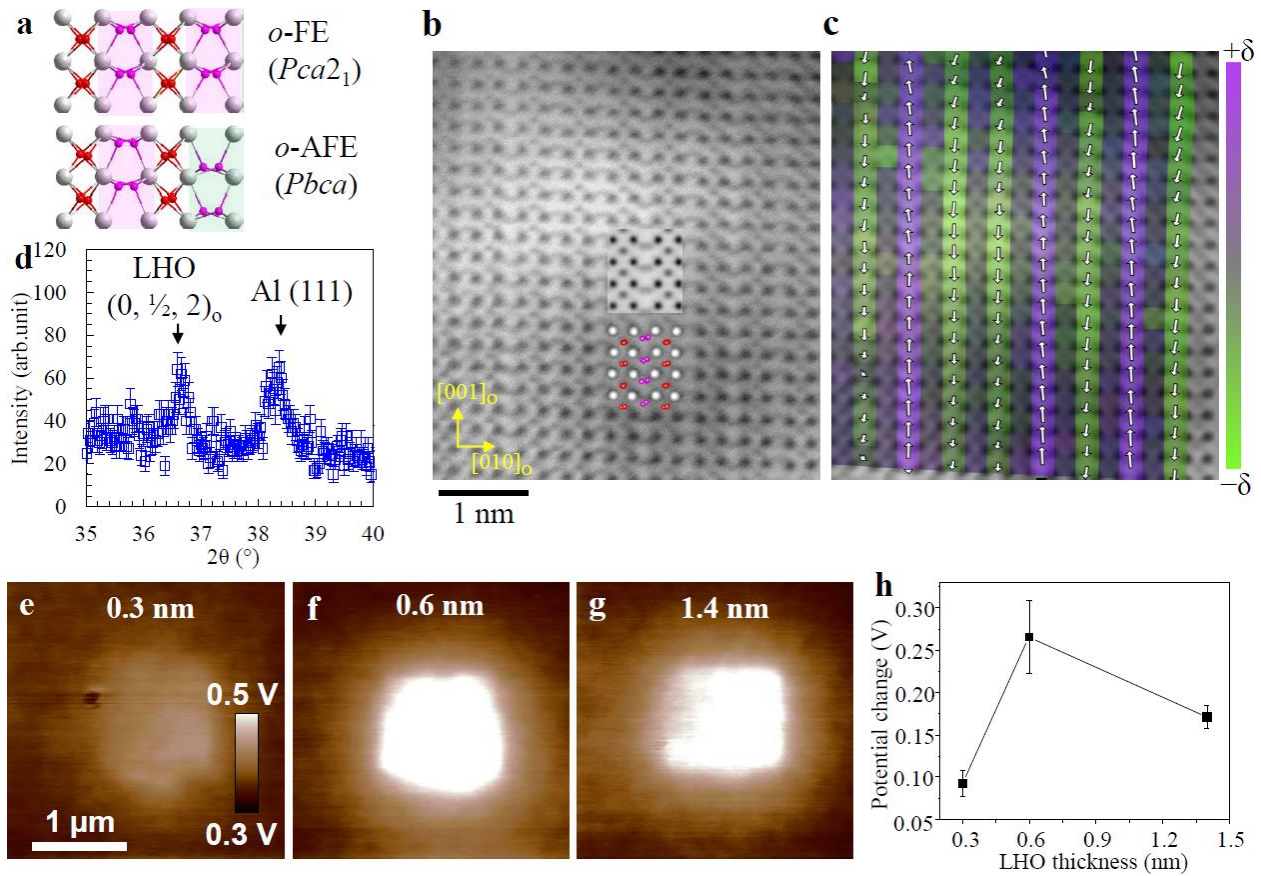


Figure 2. Polar domain structures and evidence of mechanical switching in LHO (111)/YSZ (111) films. (a) Comparison of the crystal structures of *o*-FE and *o*-AFE phases where the latter is a $1 \times 2 \times 1$ super cells of the former with the oxygen displacement in the two cells in antiparallel alignment. (b) ABF-STEM image viewed from the LHO $[100]_o$ direction, where oxygen displacement is visible. The insets are structural model (bottom) and the corresponding simulated ABF image (top). (c) Domain structure of LHO where the arrow (and color) indicates oxygen displacement δ . (d) Neutron diffraction near $(0, \frac{1}{2}, 2)_o$, consistent with the widespread of the *o*-AFE phase. (e-g) KPFM images after mechanical writing of a 1500 nN load in the center $1 \times 1 \mu\text{m}^2$ regions on the LHO films of 0.3, 0.6, and 1.4 nm respectively. (h) Potential change (ΔV) after mechanical writing as a function of the LHO film thickness.

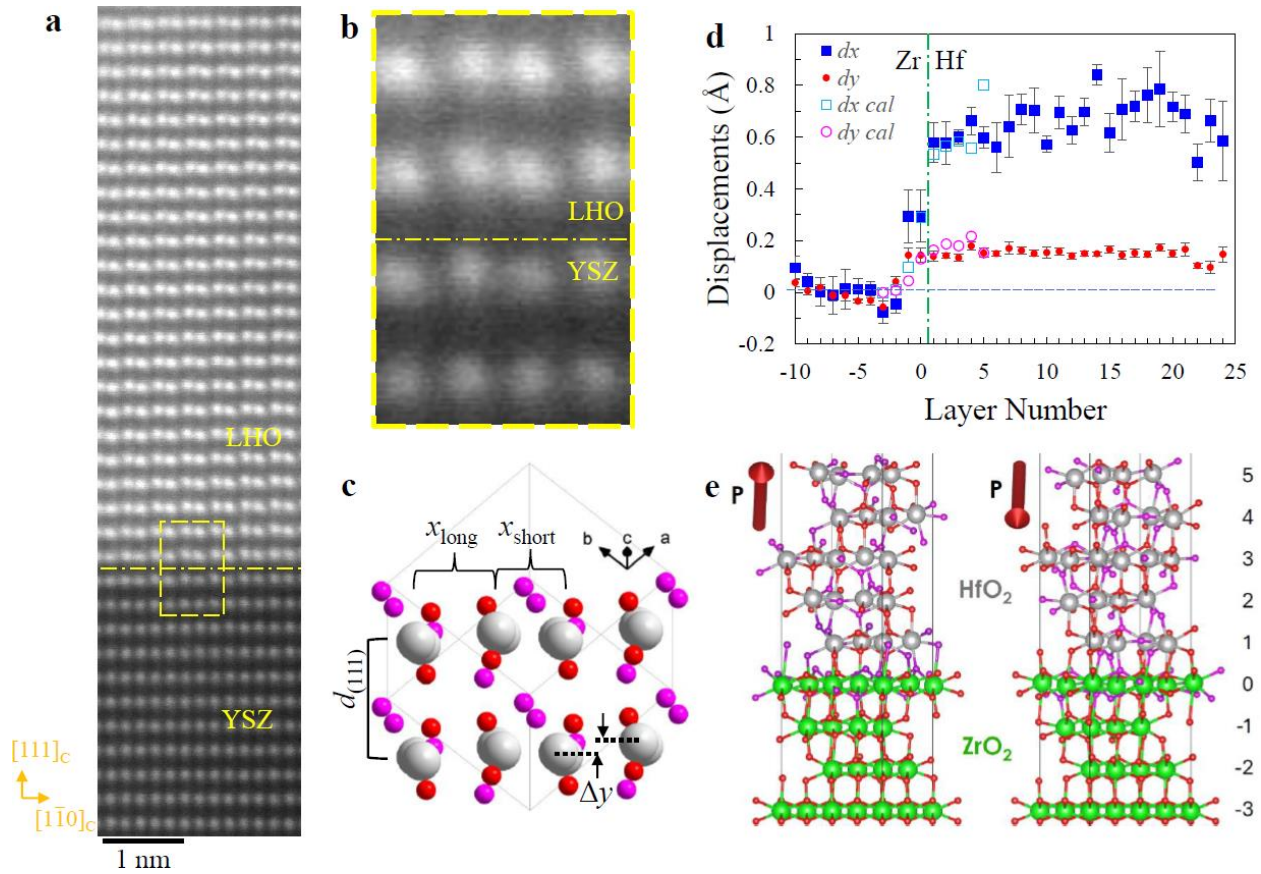


Figure 3. Structural distortions at the LHO (111)/YSZ (111) interface. (a) HAADF-STEM images viewed from the YSZ $[11\bar{2}]$ direction. (b) Closeup view of the dashed box in (a), where the structural dimerization is visible. (c) Structural model for the dimerization, which can be described by x_{long} , x_{short} , and Δy . (d) Experimental and theoretical values of $\Delta x \equiv x_{\text{long}} - x_{\text{short}}$ and Δy . (e) Interfacial structure found from the DFT calculation (see text).

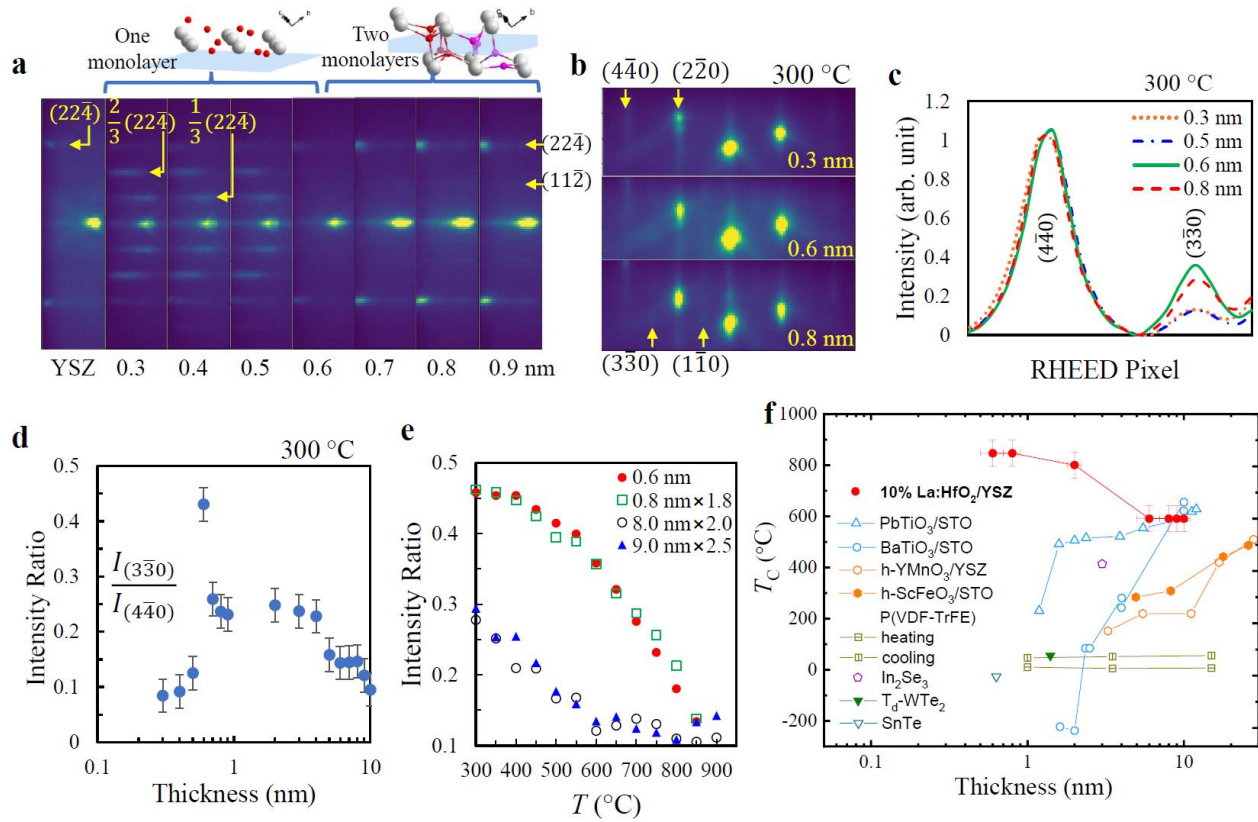


Figure 4. Thickness and temperature dependence of orthorhombic order of the LHO (111) / YSZ (111) films. (a) and (b) are evolution of RHEED patterns with increasing film thickness, with the e-beam along the $[1\bar{1}0]$ direction and $[11\bar{2}]$ directions respectively. (c) Intensity profile of RHEED of different film thicknesses. (d) $I_{(3\bar{3}0)}/I_{(4\bar{4}0)}$ as a function of film thickness. (e) $I_{(3\bar{3}0)}/I_{(4\bar{4}0)}$ as a function of temperature showing transition between the o phase and the t phase. The data for 0.8 nm, 8.0 nm, and 9.0 nm are scaled. (f) Comparison of thickness dependence of the Curie temperature between different ferroelectric systems.